RSC Applied Interfaces

ROYAL SOCIETY OF CHEMISTRY

PAPER

View Article Online
View Journal | View Issue

Cite this: *RSC Appl. Interfaces*, 2024, **1**, 992

Engineering Pt–CeO_2 interfaces for reverse water-gas shift (RWGS) reaction†

Kauê G. G. dos Santos,[a] Alisson S. Thill, [a] Livia P. Matte, [a] Gustavo Z. Girotto,[a] Mateus V. Costa,[a] Denise R. Bohn, [b] Fernanda Poletto [b] and Fabiano Bernardi *[a]

Received 26th February 2024,
Accepted 24th April 2024

DOI: 10.1039/d4lf00064a

rsc.li/RSCApplInter

Nowadays, Pt–CeO_2 interfaces are very popular in many applications. In particular, this system is widely used in catalysis for the reverse water gas-shift (RWGS) reaction aiming to stop the dangerous advancement of the global warming effect. Nevertheless, some complex atomic events occurring at this interface are still unclear. In this work, superhydrophobic Pt–CeO_2 nanoparticles were used in the RWGS reaction aiming to shift the equilibrium of the RWGS reaction towards the formation of CO. It was demonstrated that this sample presents a highly reducible CeO_2 surface and an easy tunability of the O vacancy population, which is the main active site of metal oxides in catalysis. Consequently, the Pt–CeO_2 superhydrophobic sample presents improved performance towards CO formation in the RWGS reaction. During the RWGS reaction, the Pt nanoparticles suffer from the strong metal–support interaction (SMSI) effect that may hinder the catalytically active sites but, even so, the superhydrophobic Pt–CeO_2 nanoparticles are active in the RWGS reaction. It opens new frontiers in the engineering of active superhydrophobic Pt–CeO_2 interfaces with tunable O vacancy population.

Introduction

Carbon dioxide (CO_2) is currently depicted as the most influential greenhouse gas responsible for global warming, primarily due to its high concentration in the atmosphere. The consequences of global warming include an increase in infectious diseases, a rise in sea level, and an increase in heat waves and other natural catastrophes like hurricanes.[1–3] Considering this, in the last few decades, a great deal of research has been conducted to either capture or dissociate the CO_2 molecule.[4,5] A promising approach for dissociating the CO_2 molecule is through the reverse water gas-shift (RWGS) reaction. The CO produced can be captured and utilized as a raw material for a variety of processes, such as the synthesis of polymers, hydrocarbons, and other valuable compounds like methanol, as well as a feedstock for renewable energy sources. However, the current catalysts employed in the RWGS reaction, such as Pt/CeO_2, still operate at elevated temperatures, typically around 600 °C, and exhibit limited reactivity.[6–9] Consequently, it restricts the use of the RWGS reaction against the global warming effect, thus impairing the advancement towards a healthy world.

The best way to design improved catalysts for the RWGS reaction is to make a detailed description of the atomic events occurring during the reaction. The catalytic reaction depends on different phenomena like sintering, coking, poisoning, *etc.* In particular, the occurrence of the strong metal–support interaction (SMSI) effect,[10] a famous metal/metal oxide interface effect, is closely related to the performance of the catalyst. The geometrical factor of the SMSI effect corresponds to the formation of a capping layer coming from the support and covering the metallic nanoparticles during the reduction treatment. Consequently, a strong change in the catalytically active sites available occurs at the surface of the nanoparticles, thus improving or impairing the catalytic activity.[11,12] Given the above, it is crucial to determine the interface effects occurring during the RWGS reaction and their influence on the catalytic reaction.

Pt/CeO_2 nanoparticles are relatively good catalysts for the RWGS reaction. In particular, CeO_2 can easily alternate between its totally reduced (Ce(III), Ce_2O_3) and fully oxidized (Ce(IV), CeO_2) states repeatedly.[13] Oxygen vacancies work as adsorption sites for CO_2 molecules during the RWGS reaction, so CeO_2 is an interesting support for the reaction.[14] An interesting idea is the use of hydrophobic supports for the reversible RWGS reaction. It allows shifting the RWGS equilibrium towards the formation of CO products, thus

[a] *Programa de Pós-Graduação em Física, Instituto de Física, Universidade Federal do Rio Grande do Sul, Brazil. E-mail: bernardi@if.ufrgs.br*
[b] *Programa de Pós-Graduação em Química, Instituto de Química, Universidade Federal do Rio Grande do Sul, Brazil*

† Electronic supplementary information (ESI) available. See DOI: https://doi.org/10.1039/d4lf00064a

increasing the dissociation efficiency of the CO_2 molecule. However, it is hard to find studies reporting the hydrophobicity property of metal oxide supports used in the RWGS reaction. In this work, to enhance the reactivity of Pt–CeO_2 nanoparticles towards CO formation in the RWGS reaction at low temperatures, superhydrophobic CeO_2 nanoparticles were synthesized and used together with Pt nanoparticles.

Experimental

Superhydrophobic CeO_2 nanoparticles were synthesized using the precipitation method. Firstly, $Ce(OH)_3$ nanoparticles were synthesized in a lyotropic liquid-crystalline medium composed of phytantriol and water, using $Ce(NO_3)_3{\cdot}6H_2O$ as a precursor. In a round-bottom flask, 2.40 g of phytantriol and 0.24 g of the precursor $Ce(NO_3)_3{\cdot}6H_2O$ were added. This mixture was treated with NaOH and subsequently with H_2O_2, as previously described,[15] to obtain CeO_2 nanoparticles. After this treatment, the mixture was dissolved in 10 ml of absolute ethanol and kept under gentle magnetic stirring for 8 h. After this period, the mixture was allowed to stand for 12 h. Subsequently, centrifugation was carried out at 3500 rpm for 15 min. The precipitated powder was separated by decantation, washed with a fresh aliquot of 8 ml of absolute ethanol, and centrifuged under the same previously described conditions. This process was repeated three times. After ethanol extractions, the precipitate was washed with 8 ml of Milli-Q water and centrifuged for 15 min at 3500 rpm. The remaining precipitate was kept in a desiccator under reduced pressure for 12 h for drying. The obtained powder exhibited a characteristic yellowish color. This sample will be hereafter named CeO_2 Hyd. For comparison purposes, high surface area CeO_2 nanoparticles were also synthesized in accordance with previous work,[16] hereafter named CeO_2 high S. In this case, 2 g of $(NH_4)_2Ce(NO_3)_6$ dissolved in 6 ml of distilled water was added dropwise to a saturated aqueous solution (14 mL) of ammonium carbonate under magnetic stirring. The pH value of the mixture was maintained at 9 by adding excess $(NH_4)_2CO_3$. After 30 min, the resultant solution was filtered and a 2 ml aliquot of the sample was mixed with 2 ml of ethanol under magnetic stirring at 70 °C for 16 h. Nanoparticles that precipitated after this period were washed 3 times with water, centrifuged and left in a drying oven at 90 °C for 48 h. A commercial standard of CeO_2 (Sigma-Aldrich code 211575) was also used and it is named CeO_2 Std in this work.

A commercial aqueous solution (Sigma Aldrich code 773875) containing dispersed Pt nanoparticles was mixed with the different CeO_2 samples used in this work. In separate crucibles, 1 ml of the Pt aqueous solution and 19.5 mg of each CeO_2 sample were added to obtain 8 wt% Pt–CeO_2 nanoparticles. The crucibles were placed in an ultrasonic bath for 5 minutes to achieve a homogeneous mixture between Pt and CeO_2. The mixture was dried under vacuum at room temperature in a desiccator for 24 hours. After this, 1 ml of absolute ethanol was added to each crucible, and the mixture was again homogenized by ultrasonic treatment and dried in a desiccator for 3 hours more. This process was repeated three times. It resulted in a powder consisting of Pt nanoparticles mixed with CeO_2 nanoparticles.

The wettability of the CeO_2 samples was determined using contact angle measurements. For the measurements, about 10 mg of the nanoparticle powder was used to produce a homogeneous thin membrane supported on PVDF (polyvinylidene difluoride). Aiming to produce these membranes, the nanoparticle powder was sieved using a nylon mesh of 10, 25, or 40 μm size. Then, 10 mg of the nanoparticle powder was dispersed in isopropyl alcohol utilizing an ultrasound device, resulting in a homogeneous solution. A clean membrane was fixed between a glass funnel and a glass tube using a grapple. The solution was dropped inside the glass tube and, with the help of a vacuum pump attached to the glass funnel, passed through the membrane forming a thin layer of the nanoparticle powder on the membrane. The membrane was fixed on the sample holder for the contact angle measurements. A drop of 0.2 μl, 0.3 μl, or 0.5 μl of Milli-Q water was dropped over the membrane. For each drop volume, the procedure was repeated at least 10 times for all the different grain sizes (10, 25 and 40 μm). The contact angle value was determined through the Surftens software. The final contact angle was the average value obtained from the different measurements.

Transmission Electron Microscopy (TEM) images were obtained for the Pt and CeO_2 nanoparticles in a JEOL JEM 1200 EXll microscope with an operating voltage of 80 kV at CMM BR-Sul-UFRGS. A drop of the aqueous solution containing the nanoparticles was dropped over a carbon-coated copper grid. The grid was left to dry before the TEM measurements. The size of the nanoparticles was manually obtained using ImageJ software. For each nanoparticle, two width measurements in perpendicular directions were taken and averaged to determine the nanoparticle diameter. High-Resolution TEM (HRTEM) images were obtained for the Pt–CeO_2 nanoparticles using a Tecnai G2-20 – FEI SuperTwin microscope with an operating voltage of 200 kV at CM-UFMG. The samples were prepared with the same procedure used for the TEM measurements.

Small Angle X-ray Scattering (SAXS) measurements were conducted in the aqueous solution containing the Pt nanoparticles on the Nano-inXider (Xenocs) equipment at CNANO-UFRGS. A Cu Kα X-ray source with a wavelength of 1.54 Å and a Dectris Pilatus 3 detector with a semitransparent beamstop were used in the measurements. The aqueous solution containing the Pt nanoparticles was inserted in a borosilicate tube with a 2 mm external diameter, 80 mm length and 0.01 mm thickness. The measurements were performed in transmission mode in the 2θ range from 0.00° to 5.25° with a 60 s exposure time for each scan. The final pattern resulted from an average of 60 scans.

The Foxtrot software was used to convert symmetric 2D SAXS data into 1D data and to obtain the average between multiple scans.[17] SAXS patterns were analyzed using the SASfit software.[18] Raw SAXS data were subtracted by the background function

$$I(q) = c_0 + c_1 q + c_4 q^{-\alpha} \quad (1)$$

which was adjusted to achieve the best parameters. The alpha value achieved was 3.6. The fitting procedure was conducted using a log-normal size distribution of spherical particles.

Rutherford Backscattering Spectrometry (RBS) measurements were performed to determine the Pt amount deposited on each CeO_2 sample. The RBS measurements were conducted at a TANDETRON 3 MV accelerator at the Laboratório de Implantação Iônica-UFRGS with a He beam of E_0 = 2 MeV. The scattered ions were detected at θ = 165°. The measurements were conducted in a pressure of 10^{-6} mbar and with an ion current of around 10 nA. The amount of Pt supported on each sample was quantified using the following equation:

$$\frac{N_{Pt}}{N_{Ce}} = \frac{H_{Pt}}{H_{Ce}} \frac{{Z_{Ce}}^2}{{Z_{Pt}}^2} \frac{\varepsilon_{Pt}}{\varepsilon_{Ce}} \quad (2)$$

where N represents the molar concentration of each element, H denotes the counts at the plateau for each element in the RBS spectrum, Z stands for the atomic number, and ε is the stopping cross-section factor, which was determined from the stopping power value obtained in the SRIM software.[19]

X-ray Photoelectron Spectroscopy (XPS) measurements were performed in the as-prepared Pt–CeO_2 nanoparticles at the Laboratório Nacional de Nanotecnologia (LNNano – CNPEM) with a Thermo Scientific K-α X-ray photoelectron spectrometer using an Al Kα X-ray source ($h\nu$ = 1486.6 eV) operating at 12 kV and with a 45° emission angle of the photoelectrons with respect to the incident X-rays. For the measurements, a thin layer of powder from each sample was dispersed on a carbon tape, attached to the sample holder, and introduced in an ultrahigh vacuum chamber (1×10^{-9} mbar). The measurements were performed in the survey, Pt 4f, Ce 3d, C 1s, and O 1s electronic regions of the samples. The measurements were conducted with an energy step of 0.33 and 0.05 eV, and a dwell time of 0.5 s, for the survey and high-resolution regions, respectively. The analyzer's energy calibration was performed using a standard Au foil (Au $4f_{7/2}$ peak at 84.0 eV). The C 1s peak position of adventitious carbon at 284.5 eV was also considered to verify possible charging effects.

The XPS data were analyzed using the XPSPeak software. In order to fit the high-resolution XPS spectra, a symmetric Gaussian–Lorentzian function with a 55% Lorentzian contribution was employed, as determined from analyzing the isolated and highest energy peak in the Ce 3d region at 916.7 eV. A Shirley-type background was used in all the cases. The FWHM values and the relative binding energy of a given component remained fixed across different measurements of different samples.

The Ce 3d XPS region was adjusted with 10 distinct components, where four of these represent the Ce(III) oxidation state and are named v_0, v', u_0, and u' and the other six components represent the Ce(IV) oxidation state and are named v, v'', v''', u, u'' and u''', as described by Schierbaum.[20] The Ce 3d XPS spectra of the samples were fitted simultaneously, constraining the FWHM and relative energy position of different spectra to be the same. The u_0/v_0 and u'/v' intensity ratios were constrained to 1.5. The surface Ce(III) fraction (μ_{surf}) was determined from this fitting using the XPS intensities as shown in eqn (3)

$$\mu_{surf} = \frac{u_0 + u' + v_0 + v'}{\sum u + v} \quad (3)$$

Fourier-Transform Infrared Spectroscopy (FTIR) measurements were performed at the Laboratório de Materiais Poliméricos (LAPOL-UFRGS) using the Spectrum 1000 Perkin Elmer equipment. The FTIR measurements were performed with 4 cm^{-1} resolution and the result is from the average of 32 scans. Sample preparation for FTIR measurements was performed by mixing the sample powder with KBr.

In situ XAS measurements were conducted at Laboratório Nacional de Luz Síncrotron (LNLS). The nanoparticle powder was mixed with boron nitride (BN) and compacted to make a homogeneous 5 mm diameter pellet before introduction into the tubular furnace existing at the beamline. The quantity of nanoparticles and BN depends on the edge probed and is described below. In all the cases, the samples were initially exposed to a reducing atmosphere with 100 ml min^{-1} 5% H_2 + 95% He flux. Then the samples were heated to 400 °C at a 10 °C min^{-1} rate under this atmosphere. At 400 °C, the samples were kept in the reducing atmosphere for 30 minutes. After this, a mixture of 75 ml min^{-1} 20% CO_2 + 80% He and 300 ml min^{-1} 5% H_2 + 95% He was introduced, initiating the RWGS reaction at a temperature of 400 °C for 1 hour. After the RWGS reaction, the samples were cooled to room temperature under 200 ml min^{-1} N_2.

In situ time-resolved XANES (X-ray Absorption Near Edge Structure) measurements at the Ce L_3 edge (5723 eV) were performed in transmission mode at the DXAS beamline at LNLS.[21] For the measurements, pellets containing 8 mg of Pt–CeO_2 nanoparticle powder mixed with 40 mg of BN were inserted into the tubular furnace. The XANES spectra were collected every 18 s during the full reduction treatment and RWGS reaction. The measurements made use of a curved Si(111) crystal (dispersive polychromator) and a CCD detector. The time resolution of the measurements was 100 ms. The *in situ* time-resolved XANES measurements were performed simultaneously with time-resolved mass spectrometry measurements to correlate the CeO_2 oxidation state with the sample's reactivity.

The reduction and reactivity of the nanoparticles toward CO_2 dissociation were investigated by time-resolved mass spectrometry measurements during the *in situ* time-resolved XANES measurements described. The reaction products were analyzed using a Pfeiffer Vacuum OmniStar mass spectrometer coupled to the tubular furnace. To remove possible signal fluctuations coming from the flux variations on the inserted gas, the signal from CO (m/q = 28) was normalized by the He (m/q = 2) signal detected, where m/q denotes the mass/charge ratio since He is an inert gas and it is not interacting with the sample and the H_2/He and CO_2/He ratios are fixed. The reactivity towards the formation of CO was determined through the CO/CO_2 signal ratio normalized by the Pt–CeO_2 mass of the sample.

The *in situ* time-resolved XANES spectra were fitted using a linear combination of arctangent and Lorentzian functions, as described by Takahashi *et al.*[22] For this fitting, XANES spectra of Ce(IV) and Ce(III) standards were fitted with two and one Lorentzian function, respectively. It also used an arctangent function with the same parameters for both standards. In this way, it was possible to obtain the parameters (width and position) of the arctangent and Lorentzian functions for the Ce(IV) and Ce(III) standards that were then used as fixed parameters for the fitting of the *in situ* XANES spectra of the samples. Only the height of each Lorentzian function was varied in the fitting procedure of each XANES spectrum of the samples. The Ce(III) fraction (μ) was calculated by using eqn (4)

$$\mu = 1 - \frac{A_4}{A_3 + A_4} \quad (4)$$

where A_3 and A_4 are the areas of the Lorentzian functions associated with the Ce(III) and Ce(IV) components, respectively.

In situ Extended X-ray Absorption Fine Structure (EXAFS) measurements were performed at the Pt L_3 edge (11 564 eV) in transmission mode at the XAFS2 beamline at LNLS[23] to investigate the local atomic order around the Pt atoms during the thermal treatment. For the measurements, pellets containing 15 mg of Pt–CeO_2 nanoparticle powder mixed with 40 mg of BN were inserted into the tubular furnace. In this beamline, the radiation emitted by a bending magnet was first collimated vertically by a Rh-coated cylindrical mirror, then the beam was monochromatized by a Si(111) double crystal monochromator and focused in the sample by a second Rh-coated mirror. The *in situ* EXAFS spectra were collected at the end of each gaseous treatment to ensure the achievement of a steady state of the sample (checked by short *in situ* XANES measurements). The measurements were performed using three ionization chambers filled with Ar. Standard Pt foil was used to calibrate the Si(111) monochromator. The spectra were acquired in the range of 11 610–12 025 eV with 0.5 and 1 eV per steps and 2 s per point and 3 s per point for the XANES and EXAFS regions, respectively. Two to four scans were collected to improve the signal-to-noise ratio.

The EXAFS spectra were analyzed in accordance with the standard procedure of data reduction using IFEFFIT.[24,25] The k^2-weighted EXAFS signal $k^2\chi(k)$ was extracted and then Fourier transformed using a Kaiser–Bessel window with a k range of 8.0 $Å^{-1}$. The phase shift and amplitudes were obtained with the FEFF6 code[26] by using metallic Pt, PtO_2, and H_2PtOH_6 clusters of 6 Å radius. Single scattering events were considered in the fitting procedure of the coordination shell. The $S_0{}^2$ value was fixed at 0.7 as obtained from the fitting of the Pt standard. The R-factor obtained from the analysis was always lower than 0.03, which demonstrates the excellent agreement between the proposed model and the experimental result.

Results and discussion

A typical TEM image of the Pt nanoparticles is shown in Fig. 1a, where it is possible to observe small nanoparticles with a mean diameter of 2.4 ± 0.4 nm and an almost circular projection in the plane. The SAXS pattern of the Pt nanoparticles is depicted in Fig. 1b. The big wavelength indicates the presence of small nanoparticles. The fitting result gives a lognormal size distribution of spherical particles of 3.0 ± 0.6 nm in diameter, in agreement with the TEM result. Fig. S1 of the ESI† shows the TEM images of the CeO_2 nanoparticles synthesized, which present a mean diameter of 1.2 ± 0.2 nm and a surface area of 9.2 $m^2\ g^{-1}$ (CeO_2 Hyd), a mean diameter of 3 ± 2 nm and a surface area of 201 $m^2\ g^{-1}$ (CeO_2 high S) and a mean diameter of 26 ± 24

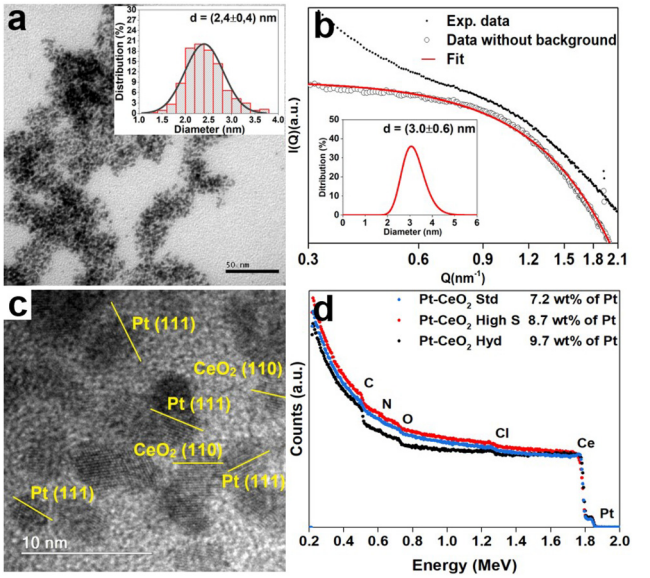

Fig. 1 a) Typical TEM image of the commercial Pt nanoparticles and the histogram of size distribution (inset). b) SAXS pattern of the commercial Pt nanoparticles and the respective fitting result with the size distribution (inset). c) Typical HRTEM image of the Pt–CeO_2 Hyd sample with the Pt and CeO_2 nanoparticles identified. d) Normalized RBS spectra of the Pt–CeO_2 Hyd, Pt–CeO_2 high S and Pt–CeO_2 Std samples in black, red and blue points, respectively.

nm and a surface area of 38 m^2 g^{-1} (CeO_2 Std). Therefore, the Pt–CeO_2 nanoparticles should consist of a mixture of Pt and CeO_2 nanoparticles of similar sizes. A typical HRTEM image of the Pt–CeO_2 Hyd sample is shown in Fig. 1c, where the presence of a uniform distribution of Pt–CeO_2 interfaces constituted of individual Pt and CeO_2 nanoparticles is observed. Furthermore, the contact angle measurement shows an average value of 157° for the CeO_2 Hyd sample (Fig. S2 of the ESI†), which demonstrates a superhydrophobic behavior of the synthesized CeO_2 sample. In the literature, it is well known that CeO_2 presents a hydrophilic nature[27] but it may become hydrophobic in nature after air exposure.[28] Despite that, it is rare to find superhydrophobic CeO_2 surfaces. The CeO_2 Std sample measured in this work is highly hydrophilic since it adsorbs the water drop. It shows that the synthesized CeO_2 Hyd sample greatly presents this unique property of superhydrophobicity, which may be highly useful for the RWGS reaction. The RBS spectra Fig. 1d show the presence of Pt, Ce, C, O, and Cl in all the samples. The Cl contamination comes probably from the Pt salt used in the synthesis process. In all the samples, the Pt amount was around 8 wt%, as expected.

The XPS measurements at the Ce 3d electronic level for the as-prepared Pt–CeO_2 samples are displayed in Fig. 2. The component labeled v''' at 916.7 eV serves as a direct indicator of the sample's oxidation state. A greater relative intensity in this component is correlated with a higher oxidation state. The Pt–CeO_2 Hyd sample presents a small intensity for this component, indicating a highly reduced sample. The surface Ce(III) fractions obtained from the fitting for the as-prepared Pt–CeO_2 nanoparticles were 0.77, 0.33, and 0.25 for the Pt–CeO_2 Hyd, Pt–CeO_2 high S, and Pt–CeO_2 Std samples, respectively. The CeO_2 nanoparticles synthesized in this work exhibited a high surface Ce(III) fraction in comparison to the literature,[29–31] which is typically around 0.1. The high surface Ce(III) fraction values, especially for the Pt–CeO_2 Hyd sample, give a large O vacancy population, which are the most active sites of metal oxides for catalysis.[32] It is another promising result for using the synthesized nanoparticles in the RWGS reaction.

In the Pt 4f region, a consistent chemical environment around Pt atoms was observed across all the samples. A small metallic Pt component at 70.9 eV[33] was detected, followed by the main contribution from $Pt(OH)_x$ at 73.0 eV[33] coming from the surfactant present at the Pt nanoparticle surface. However, the posterior activation treatment, typically employed in catalysis, should be able to remove it and leave the Pt nanoparticles ready for the catalytic reaction.

The chemical components at Pt–CeO_2 interfaces were studied by C 1s XPS measurements (Fig. S3 of the ESI†). In addition to the adventitious carbon, the presence of CO adsorbed at the CeO_2 surface is observed in all the samples coming from air exposure. Interestingly, only the Pt–CeO_2 Std sample presents CO bonding at the Pt surface. It may be associated with the low porosity of CeO_2 in the standard sample, consequently, Pt nanoparticles are more exposed to the atmosphere and subjected to the formation of CO bonding at the surface. The CH_3OH component appears due to the ethanol used during the synthesis process of CeO_2. The phytantriol component in the C 1s XPS spectrum is expected at 282.7 eV due to the presence of highly reduced C atoms in the structure,[34] but it is not observed in the Pt–CeO_2 Hyd sample. FTIR measurements (Fig. S4 of the ESI†) were also conducted and the spectra are consistent with the findings in the XPS measurements. Moreover, it shows the absence of the characteristic bands of phytantriol.[35]

Mass spectrometry measurements were performed during the RWGS reaction. Fig. 3 shows the reactivity of the nanoparticles towards the formation of CO. The zero on the *x*-axis represents the beginning of the RWGS reaction at 400 °C. The reactivity of Pt–CeO_2 Hyd, Pt–CeO_2 high S, and Pt–CeO_2 Std nanoparticles was determined as approximately 10%, 8%, and 3%, respectively. The Pt–CeO_2 Hyd sample exhibits a much higher reactivity than the Pt–CeO_2 Std sample and higher reactivity than the Pt–CeO_2 high S sample, thus showing that the use of superhydrophobic nanoparticles

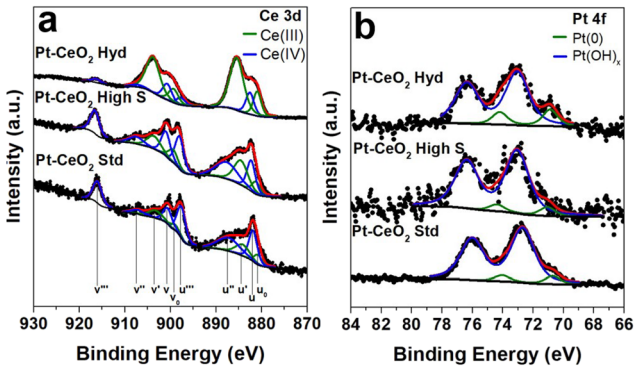

Fig. 2 High resolution XPS spectra at a) Ce 3d and b) Pt 4f XPS regions of the as-prepared Pt–CeO_2 nanoparticles.

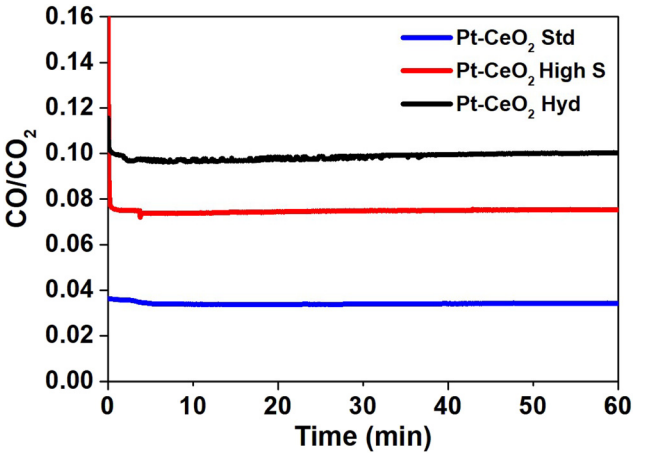

Fig. 3 Normalized signal of the CO/CO_2 ratio as a function of time during the RWGS reaction.

results in increased reactivity for the RWGS reaction. In fact, the experiment was repeated for the CeO_2 Hyd sample (without Pt) to investigate the effect of superhydrophobicity on the CO and H_2O product formation. At 400 °C, the RWGS reaction started and a temperature-dependent study was conducted, heating the sample to 500 °C during the RWGS reaction. An increase of the reactivity with the temperature is expected, and a constant H_2O/CO ratio due to the stoichiometry of the reaction. However, there is a strong drop to half of the value of the H_2O/CO ratio with the increase of the temperature (Fig. S5a of the ESI†). It occurs because H_2O molecules are bounded at the CeO_2 surface due to the loss of the superhydrophobicity property of CeO_2. Consequently, more CO molecules are detected at the mass spectrometer than H_2O molecules and the H_2O/CO ratio drops. Moreover, the reactivity starts to decrease as well (Fig. S5b of the ESI†), which shows that the loss of superhydrophobicity property impairs the reactivity towards CO production. It means that, indeed, the superhydrophobicity property helps on the reactivity towards CO formation. It is interesting to note that the Pt–CeO_2 Hyd sample presents a smaller surface area than the Pt–CeO_2 high S sample (9.2 m^2 g^{-1} against 201 m^2 g^{-1}) but, even so, the superhydrophobicity property is enough to improve the reactivity of the nanoparticles. The reactivity normalized by the surface area gives a more realistic comparison between the samples since it allows evaluation of the performance of the active sites on each surface, despite the different amounts of active sites. This value for the Pt–CeO_2 Hyd sample is almost 30 times bigger than the Pt–CeO_2 high S one, which demonstrates the great advancement achieved in the present work. Furthermore, the reactivity towards CO formation is stable at least during 1 h of RWGS reaction.

Fig. S6 of the ESI† shows the H_2O/CO ratio as a function of time obtained from mass spectrometry measurements during the RWGS reaction to identify whether the superhydrophobic property of the Pt–CeO_2 Hyd sample is lost during the reaction at 400 °C. The result presents an almost constant H_2O/CO ratio during the RWGS reaction, which shows that the superhydrophobic property was not lost during 1 h of RWGS reaction at 400 °C. The small increase observed (close to 3%) in the Pt–CeO_2 Hyd sample occurs in the Pt–CeO_2 high S sample (hydrophilic) as well and it is attributed to H_2O molecules trapped at the connection walls of the mass spectrometer system. Thus, at least during 1 h of RWGS reaction at 400 °C, there is no evidence of the Pt–CeO_2 Hyd sample losing the superhydrophobicity property. However, the increase of temperature induces the loss of the superhydrophobicity property, as shown in Fig. S5 of the ESI.†

Fig. 4 shows typical *in situ* time-resolved XANES spectra at the Ce L_3 edge of the Pt–CeO_2 samples. The spectra are shown every 5 min during the heating stage of the thermal treatment since this is the range of bigger changes observed. Fig. S7 of the ESI† shows the *in situ* time resolved XANES spectra at 400 °C, where no significant changes are observed. It can be observed that initially, all the samples exhibit a doublet, characteristic of the Ce(IV) oxidation state, although with visually different intensity ratios, which should imply different initial oxidation states. After starting the reduction treatment of the samples in the H_2 atmosphere, a clear qualitative change from the Ce(IV) to Ce(III) oxidation state is observed in the Pt–CeO_2 Hyd sample, with the appearance of a singlet, characteristic of the Ce(III) oxidation state, and a slight decrease in the height of the second peak in the Pt–CeO_2 high S sample. The Pt–CeO_2 Std sample does not show significant changes in the oxidation state during the reduction treatment. The Ce(III) fraction as a function of time, obtained from the analysis of the *in situ* XANES spectra of the three samples, is shown in Fig. 4d. Fig. S8 of the ESI† shows a typical fit result from the analysis conducted. During the heating process, all the samples showed a continuous increase in the Ce(III) fraction, except for the Pt–CeO_2 Hyd sample, which stabilizes its oxidation state before reaching 400 °C. In a previous study,[16] highly reducible CeO_2 nanoparticles were synthesized. The nanoparticles were reduced at temperatures as low as 110 °C when exposed to a CO atmosphere. In particular, CeO_2 high S nanoparticles presented a reduction temperature (defined as the inflection point of the curve of the Ce(III) fraction as a function of time) of 188 °C. In the present study, CeO_2 high S nanoparticles presented a reduction temperature of 202 °C under H_2 atmosphere, which makes sense since CO presents a higher reducing power than the H_2 molecule in the CeO_2 to Ce_2O_3 reduction reaction. The Ce(III) fraction values found are much higher than typical values from the literature for the Pt/CeO_2

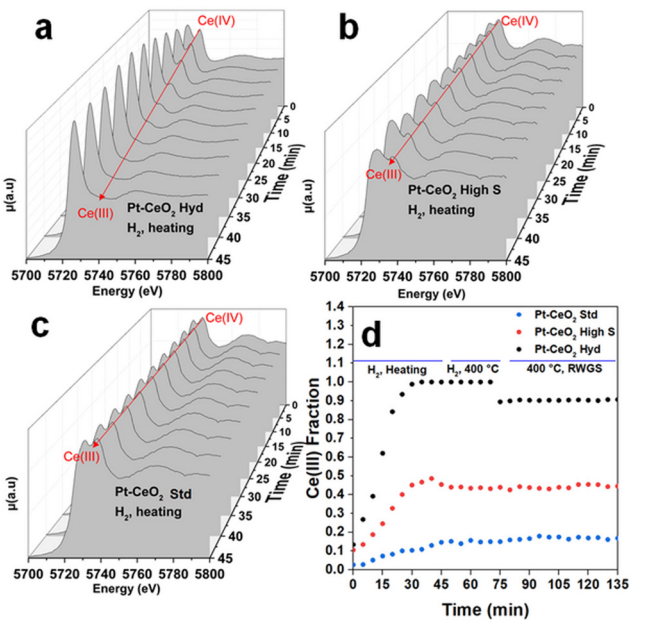

Fig. 4 Time evolution of the *in situ* XANES spectra at the Ce L_3 edge during heating treatment to 400 °C under H_2 atmosphere for a) Pt–CeO_2 Hyd, b) Pt–CeO_2 high S and c) Pt–CeO_2 Std samples. d) Time evolution of the Ce(III) fraction in the Pt–CeO_2 samples during reduction and RWGS reaction.

system after reduction treatment.[29–31] In particular, Pastor-Pérez *et al.* achieved 37% of Ce(III) after reduction treatment at almost the same temperature used here (350 °C).[31] In the present study, the Pt–CeO_2 high S sample presents a higher Ce(III) fraction of 48%, and Pt–CeO_2 Hyd is even more reduced with 98% of Ce(III) fraction. It is interesting to note that Pt/CeO_2 nanoparticles should present the electronic effect of SMSI where a charge transfer from Pt to CeO_2 is observed, thus helping with CeO_2 reduction.[30] For Pt–CeO_2 Hyd nanoparticles, a much lower reduction temperature of 152 °C is found. It does not occur due to the charge transfer from Pt nanoparticles to CeO_2 since the same experiment was repeated for CeO_2 Hyd nanoparticles without Pt nanoparticles and almost the same reduction temperature was found (not shown here). In fact, H_2-TPR measurements were conducted with the monitoring of the H_2O signal using a mass spectrometer during sample reduction (Fig. S9 of the ESI†). The results point to Pt reduction from $Pt(OH)_x$ to Pt(0) starting at low temperatures of around 50 °C for all the samples. The Pt nanoparticles are fully reduced at around 175 °C. The reduction process of CeO_2 starts at different temperatures. Pt–CeO_2 Hyd starts to reduce earlier, followed by Pt–CeO_2 high S and then the Pt–CeO_2 Std sample, in accordance with the time evolution of the Ce(III) fraction (Fig. 4). It is consistent with a Pt–CeO_2 interaction through charge transfer from Pt to CeO_2, as previously reported,[30] but the different extent on CeO_2 reduction comes from the surface properties of the nanoparticles synthesized. This result shows the existence of easily reduced CeO_2 nanoparticles, thus presenting plenty of oxygen vacancies, which are great active sites of metal oxides in catalysis (not restricted to the RWGS reaction).

At 400 °C, the Ce(III) fraction becomes constant and stable in all the samples. During the RWGS reaction, the Ce(III) fraction remains the same in the Pt–CeO_2 high S and Pt–CeO_2 Std samples, while it slightly decreases by 10% in the Pt–CeO_2 Hyd sample. Besides a small reduction, it occurs only at the beginning of the RWGS reaction and the Ce(III) fraction remains the same during 1 h of RWGS reaction. It indicates that the CO_2 molecules are readily adsorbed at CeO_2, then slightly oxidizing it, but it stabilizes quickly for the remaining time of reaction. It is observed that there is a direct relation between the reactivity towards CO formation and the O vacancy population in the CeO_2 nanoparticles. The higher the O vacancy population, the higher the reactivity towards CO formation. In the literature it is possible to find studies reporting on the activation of CO_2 in the RWGS reaction through the interaction between Pt and CeO_2,[36] frustrated Lewis pairs[37] or O vacancies at the CeO_2 surface.[38] The slight oxidation of CeO_2 in the Pt–CeO_2 Hyd sample after CO_2 insertion and the relation between reactivity towards CO formation and Ce(III) fraction indicates that the activation of CO_2 occurs at the O vacancies of the CeO_2 surface in this case. Then, in addition to the superhydrophobicity of the Pt–CeO_2 Hyd sample, its great reducibility makes it highly interesting for catalytic applications. Considering this, the

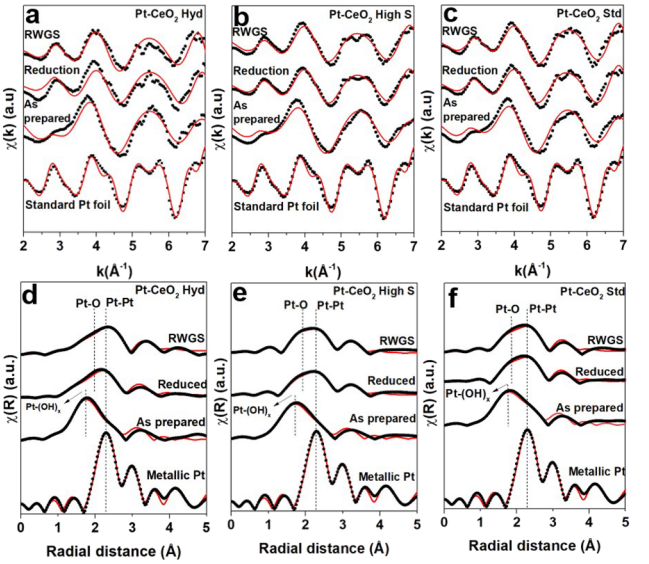

Fig. 5 EXAFS oscillations from *in situ* EXAFS measurements at the Pt L_3 edge of the as-prepared Pt–CeO_2 samples, during reduction treatment and RWGS reaction (a–c) and the respective Fourier transform (d–f). The best fitting found is represented by the red line.

Pt–CeO_2 Hyd sample is highly promising for future applications due to the high reactivity towards CO formation at a relatively low temperature and easy tunability (through the low temperature used) of the Ce oxidation state.

Fig. S10 of the ESI† shows the normalized *in situ* XAS spectra at the Pt L_3 edge of the as-prepared Pt–CeO_2 samples, during reduction treatment and RWGS reaction. It can be observed that initially, all spectra present high intensity right after the absorption edge, which is linked to a non-metallic state of Pt. This is in accordance with the XPS measurements at the Pt 4f electronic region. During the reduction treatment, the spectra of all the samples clearly changed to a metallic state, as expected. It is very similar to the findings reported in the literature.[29] There is no further significant qualitative alteration observed during the RWGS reaction. The fitting of the XANES spectra with a linear combination of Pt and PtO_2 standard spectra resulted in 100% Pt during both reduction and RWGS reactions.

Fig. 5 illustrates the k^2-weighted EXAFS oscillations and the respective FT from *in situ* EXAFS measurements at the Pt L_3 edge. The EXAFS oscillations of the as-prepared samples show a distinct pattern compared to that presented in the Pt foil. After reduction, the EXAFS oscillations are typical of metallic Pt but they are damped due to the high temperature of analysis. A comparison between the Fourier transform of the as-prepared Pt–CeO_2 samples and the standard metallic Pt foil clearly reveals that the as-prepared Pt nanoparticles are not fully reduced since there is an important contribution at short distances from a Pt–OH scattering path. This statement is supported by the XPS measurements at the Pt 4f region, where a small metallic component was observed, followed by a huge contribution from hydroxyl groups bound to the Pt atoms. During reduction treatment, there is an

increase in the intensity around 2.2 Å and 2.0 Å (not phase corrected), which are associated with Pt–Pt and Pt–O scattering paths, respectively, together with the disappearance of the Pt–$(OH)_x$ scattering. This indicates that the Pt atoms are reduced due to the thermal treatment applied, but a Pt–O component is still present.

Table S1 of the ESI† presents the parameters found during the fitting process described for the three samples. The Pt–Pt coordination number of the as-prepared nanoparticles points to a rough estimation of the size of a few nm,[39] in agreement with the TEM and SAXS results. The Pt–$(OH)_x$ contribution is small when compared to the Pt–Pt one, which is consistent with the Pt–$(OH)_x$ bonding present at the surface of the nanoparticles. An increase in the coordination number associated with the Pt–Pt scattering path was also observed during reduction and RWGS reactions at 400 °C, which can be attributed to the sintering of Pt nanoparticles due to the elevated temperature.

Surprisingly, the Pt–O scattering path has an important contribution during the reduction treatment. The oxidation of Pt cannot be attributed to the gaseous atmosphere since only H_2 and He were interacting with the sample during reduction treatment. At this temperature and atmosphere, it is expected that Pt reduces easily and becomes fully metallic.[29] However, it is well known from the literature that Pt–CeO_2 nanoparticles exhibit the geometrical factor of the SMSI effect under a reducing atmosphere at elevated temperatures.[40,41] The formation of the capping layer covering the metallic nanoparticles is driven by the minimization of the surface energy.[42] Metal nanoparticles typically present surface energy much higher than metal oxides. Despite the reduced size of the CeO_2 nanoparticles as compared to typical systems in the literature, this relation still should hold due to the small size of the Pt nanoparticles as well and the typical variation of the surface energy of CeO_2 with size in this size range.[43] Then the presence of CeO_2 nanoparticles smaller than Pt nanoparticles (Pt–CeO_2 Hyd sample) should not avoid the geometrical factor of the SMSI effect whether there is indeed a Pt–CeO_2 interface, as demonstrated in Fig. 1c. This effect can be responsible for the appearance of a strong Pt–O–Ce bond,[44] which can explain the appearance of the Pt–O component. The geometrical factor of the SMSI effect may lead to a decrease or increase in the catalytic activity. Catalyst deactivation occurs due to the loss of catalytically active sites caused by the encapsulation of the metallic nanoparticles.[4,12,40] On the other hand, in some cases the encapsulating layer may create new catalytically active sites at the surface[11] that improve the catalytic activity. During the RWGS reaction, no new scattering path emerged. However, a slight increase in the coordination number associated with the Pt–O scattering path was observed. This increase is more evident in the Pt–CeO_2 Hyd and Pt–CeO_2 high S nanoparticles. The increase follows the same trend observed for the reactivity of the samples, indicating that it may come from byproducts of the RWGS reaction, especially related to the reduction of the CO_2 molecules. It indicates that the gas is interacting with the Pt nanoparticles, even if the SMSI effect is present. It shows that the SMSI effect did not deactivate the samples, which can be explained by the penetration of the gas molecules through the encapsulating layer and interaction with the metallic surface,[45] or by the presence of a partially encapsulated metallic nanoparticle. Finally, the Pt–CeO_2 Hyd nanoparticles exhibit the best reactivity, even suffering from the SMSI effect, which may be attributed to the superhydrophobicity of CeO_2 nanoparticles that shifts the reaction towards the formation of CO and its high reducibility.

Conclusions

This work demonstrated that superhydrophobic Pt–CeO_2 interfaces are highly promising for the RWGS reaction with improved results even in comparison to high surface area Pt–CeO_2 nanoparticles. The scenario is even more exciting because the superhydrophobic Pt–CeO_2 nanoparticles are highly reducible and their O vacancy population is easily tunable through the temperature used in the reduction treatment. Besides the indication of the SMSI effect, these nanoparticles are still active toward CO formation in the RWGS reaction.

Conflicts of interest

There are no conflicts to declare.

Acknowledgements

This study was funded by FAPERGS (Project Numbers 19/2551-0000703-5 and 19/2551-0001752-9), CNPq (Project numbers 19/2551-0000703-5, 19/2551-0001752-9 and 23/2551-0000177-2). K. G. G. dos S., A. S. T., L. P. M., G. Z. G., M. V. C. and F. B. thank the CNPq for the research grant. The authors also thank CNANO-UFRGS, CMM BR-Sul-UFRGS, LII-UFRGS, CEOMAT-UFRGS, LAPOL-UFRGS, LNLS, LNNano, and CM-UFMG for the use of the infrastructure.

References

1 I. Kurane, *Osong Public Health Res. Perspect.*, 2010, **1**, 4–9.
2 P. Roy, S. C. Pal, R. Chakrabortty, I. Chowdhuri, A. Saha and M. Shit, *J. Environ. Manage.*, 2023, **330**, 117–187.
3 M. Liu, G. A. Vecchi, J. A. Smith and T. R. Knutson, *npj Clim. Atmos. Sci.*, 2019, **2**, 1.
4 W. T. Figueiredo, C. Escudero, V. Pérez-Dieste, C. A. Ospina and F. Bernardi, *J. Phys. Chem. C*, 2020, **124**, 16868–16878.
5 D. H. Kim, S. W. Han, H. S. Yoon and Y. D. Kim, *J. Ind. Eng. Chem.*, 2019, **23**, 67–71.
6 A. Goguet, S. Shekhtman, R. Burch, C. Hardacre, F. Meunier and G. Yablonsky, *J. Catal.*, 2006, **237**, 102–110.
7 C.-S. Chen, W.-H. Cheng and S.-S. Lin, *Appl. Catal., A*, 2003, **238**, 55–67.
8 M. Ginés, A. Marchi and C. Apesteguía, *Appl. Catal., A*, 1997, **154**, 155–171.

9 W. Luhui, Z. Shaoxing and L. Yuan, *J. Rare Earths*, 2008, **26**, 66–70.
10 S. J. Tauster, S. C. Fung and R. L. Garten, *J. Am. Chem. Soc.*, 1978, **100**, 170–175.
11 M. Ren, K. Qian and W. Huang, *Chem. – Eur. J.*, 2019, **25**, 15978–15982.
12 L. Wang, H. Liu, Y. Liu, Y. Chen and S. Yang, *J. Rare Earths*, 2013, **31**, 969–974.
13 A. Trovarelli, *Catal. Rev.: Sci. Eng.*, 1996, **38**, 439–520.
14 F. Cao, Y. Xiao, Z. Zhang, J. Li, Z. Xia, X. Hu, Y. Ma and Y. Qu, *J. Catal.*, 2022, **414**, 25–32.
15 D. R. Bohn, F. O. Lobato, A. S. Thill, L. Steffens, M. Raabe, B. Donida, C. R. Vargas, D. J. Moura, F. Bernardi and F. Poletto, *J. Mater. Chem. B*, 2018, **6**, 4920–4928.
16 G. B. D. Mea, L. P. Matte, A. S. Thill, F. O. Lobato, E. V. Benvenutti, L. T. Arenas, A. Jürgensen, R. Hergenröder, F. Poletto and F. Bernardi, *Appl. Surf. Sci.*, 2017, **422**, 1102–1112.
17 G. David and J. Perez, *J. Appl. Crystallogr.*, 2009, **42**, 892–900.
18 I. Brebler, J. Kohlbrecher and A. F. Thünemann, *J. Appl. Crystallogr.*, 2015, **48**, 1587–1598.
19 J. F. Ziegler, M. Ziegler and J. Biersack, *Nucl. Instrum. Methods Phys. Res., Sect. B*, 2010, **268**, 1818–1823.
20 K.-D. Schierbaum, *Surf. Sci.*, 1998, **399**, 29–38.
21 J. C. Cezar, N. M. Souza-Neto, C. Piamonteze, E. Tamura, F. Garcia, E. J. Carvalho, R. T. Neueschwander, A. Y. Ramos, H. C. N. Tolentino, A. Caneiro, M. J. M.-L. N. E. Massa, J. A. Alonso and J.-P. Itié, *J. Synchrotron Radiat.*, 2010, **17**, 93–102.
22 Y. Takahashi, H. Sakami and M. Nomura, *Anal. Chim. Acta*, 2002, **468**, 345–354.
23 S. J. A. Figueroa, J. C. Mauricio, J. Murari, D. B. Beniz, J. R. Piton, H. H. Slepicka, M. F. de Sousa, A. M. Espíndola and A. P. S. Levinsky, *J. Phys.: Conf. Ser.*, 2016, **712**, 012022.
24 D. C. Koningsberger and R. Prins, *X-ray absorption: Principles, applications, techniques of EXAFS, SEXAFS and XANES*, John Wiley and Sons, 1st edn, 1987.
25 S. I. Zabinsky, J. J. Rehr, A. Ankudinov, R. C. Albers and M. J. Eller, *Phys. Rev. B: Condens. Matter Mater. Phys.*, 1995, **52**, 4.
26 M. Newville, *J. Synchrotron Radiat.*, 2001, **8**, 322–324.
27 G. Azimi, R. Dhiman, H. Kwon, A. T. Paxson and K. K. Varanasi, *Nat. Mater.*, 2013, **12**, 315–320.
28 R. Lundy, C. Byrne, J. Bogan, K. Nolan, M. N. Collins, E. Dalton and R. Enright, *ACS Appl. Mater. Interfaces*, 2017, **9**, 13751–13760.
29 S. Alayoglu, K. An, G. Melaet, S. Chen, F. Bernardi, L. W. Wang, A. E. Lindeman, N. Musselwhite, J. Guo, Z. Liu, M. A. Marcus and G. A. Somorjai, *J. Phys. Chem. C*, 2013, **117**, 26608–26616.
30 A. S. Thill, A. S. Kilian and F. Bernardi, *J. Phys. Chem. C*, 2017, **121**, 25323–25332.
31 L. Pastor-Pérez, V. Belda-Alcázar, C. Marini, M. M. Pastor-Blas, A. Sepúlveda-Escribano and E. V. Ramos-Fernandez, *Appl. Catal., B*, 2018, **225**, 121–127.
32 C. T. Campbell, *J. Sci.*, 2005, **309**, 713–714.
33 M. Peuckert, *Electrochim. Acta*, 1984, **29**, 1315–1320.
34 A. S. Thill, Development of highly promising NiO nanofoams for hydrogen storage application, *PhD Thesis*, UFRGS, 2023.
35 A. Misiûnas, Z. Talaikytë, G. Niaura and V. Razumas, *Biologija*, 2004, **4**, 26–29.
36 F. Zhang, R. A. Gutiérrez, P. G. Lustemberg, Z. Liu, N. Rui, T. Wu, P. J. Ramírez, W. Xu, H. Idriss, M. V. Ganduglia-Pirovano, S. D. Senanayake and J. A. Rodriguez, *ACS Catal.*, 2021, **11**, 1613–1623.
37 W. Li, J. Gan, Y. Liu, Y. Zou, S. Zhang and Y. Qu, *Angew. Chem.*, 2023, **135**, 56–61.
38 A. Goguet, S. Shekhtman, R. Burch, C. Hardacre, F. Meunier and G. Yablonsky, *J. Catal.*, 2006, **237**, 102–110.
39 F. Rasera, A. S. Thill, L. P. Matte, G. Z. Girotto, H. V. Casara, G. B. D. Mea, N. M. Balzaretti, F. Poletto, C. Brito and F. Bernardi, *ACS Appl. Nano Mater.*, 2023, **6**, 6435–6443.
40 J. Z. Chen, A. Talpade, G. A. Canning, P. R. Probus, F. H. Ribeiro, A. K. Datye and J. T. Miller, *J. Sci.*, 2020, **371**, 4–710.
41 M. Abid and V. Paul-Boncour, *Appl. Catal., A*, 2006, **297**, 48–59.
42 Q. Fu and T. Wagner, *Surf. Sci. Spectra*, 2007, **62**, 431–498.
43 V. Perebeinos, S.-W. Chan and F. Zhang, *Solid State Commun.*, 2002, **123**, 295–297.
44 E. A. Derevyannikova, T. Y. Kardash, A. I. Stadnichenko, O. A. Stonkus, E. M. Slavinskaya, V. A. Svetlichnyi and A. I. Boronin, *J. Phys. Chem. C*, 2019, **123**, 1320–1334.
45 F. Bernardi, M. E. Grass, Y. P. Hong, R. Chang, N. Jabeen, C. Zhang, B. W. Eichhorn, B. Seo, S. Alayoglu, Z. Hussain, S. H. Joo and Z. Liu, *Catal. Today*, 2016, **260**, 95–99.